npj | 2D materials and applications

www.nature.com/npj2dmaterials

ARTICLE OPEN

Effect of crystallinity and thickness on thermal transport in layered $PtSe_2$

Alexandros El Sachat[1]✉, Peng Xiao[1,2], Davide Donadio[3], Frédéric Bonell[4], Marianna Sledzinska[1], Alain Marty[4], Céline Vergnaud[4], Hervé Boukari[4], Matthieu Jamet[4], Guillermo Arregui[1], Zekun Chen[3], Francesc Alzina[1], Clivia M. Sotomayor Torres[1,5] and Emigdio Chavez-Angel[1]✉

We present a comparative investigation of the influence of crystallinity and film thickness on the acoustic and thermal properties of layered $PtSe_2$ films of varying thickness (1–40 layers) using frequency-domain thermo-reflectance, low-frequency Raman, and pump-probe coherent phonon spectroscopy. We find ballistic cross-plane heat transport up to ~30 layers $PtSe_2$ and a 35% reduction in the cross-plane thermal conductivity of polycrystalline films with thickness larger than 20 layers compared to the crystalline films of the same thickness. First-principles calculations further reveal a high degree of thermal conductivity anisotropy and a remarkable large contribution of the optical phonons to the thermal conductivity in bulk (~20%) and thin $PtSe_2$ films (~30%). Moreover, we show strong interlayer interactions in $PtSe_2$, short acoustic phonon lifetimes in the range of picoseconds, an out-of-plane elastic constant of 31.8 GPa, and a layer-dependent group velocity ranging from 1340 ms^{-1} in bilayer to 1873 ms^{-1} in eight layers of $PtSe_2$. The potential of tuning the lattice thermal conductivity of layered materials with the level of crystallinity and the real-time observation of coherent phonon dynamics open a new playground for research in 2D thermoelectric devices and provides guidelines for thermal management in 2D electronics.

npj 2D Materials and Applications (2022)6:32 ; https://doi.org/10.1038/s41699-022-00311-x

INTRODUCTION

Atomically-thin 2D semiconductors have attracted immense attention in the scientific community due to their exceptional layer-dependent optical, electronic, and thermal properties that open new prospects in the microelectronics industry[1]. Vertical devices consisting of one-or few-atom thick 2D materials, where heat transport usually occurs in the vertical direction, have already shown excellent performance in diodes[2], photodetectors[3], transistors[4,5], and solar cells[6]. In such devices, the interfacial thermal properties of atomically-thin layered 2D materials significantly vary depending on their thickness, interlayer interactions, and degree of bonding with the substrate. It is therefore essential to understand cross-plane thermal transport and phonon dynamics, particularly in noble metal dichalcogenides, like $PtSe_2$, due to their large potential for integration in future high-performance 2D devices[7–10].

$PtSe_2$ exhibits outstanding inherent properties, including high carrier mobility at room temperature, which is eight times larger than MoS_2[11], excellent stability to air, and resistance to oxidation, better than black phosphorous[5]. Moreover, $PtSe_2$ can be easily integrated into practical devices since it can be grown at low temperatures[12]. Together with its widely tunable bandgap[13] and layer-dependent semiconductor-to-semimetal transition behavior[14], it is considered a promising material to be employed in many electronic[5], optoelectronic[7] and thermoelectric devices[15]. For instance, Moon et al.[15]. have recently shown that band engineering by thickness modulation leads to a 50-fold enhancement of the thermopower in bilayer $PtSe_2$ nanosheets with respect to bulk $PtSe_2$. Moreover, calculated results have shown that in monolayer $PtSe_2$ compressive or tensile strain can induce significantly enhanced n- or p-type Seebeck coefficients[16]. Despite the large potential of $PtSe_2$ in thermoelectric applications, experimental studies of the intrinsic thermal properties[17] and phonon dynamics of $PtSe_2$[18] films are few and still limited.

In this work, we study the phonon dynamics and thermal properties of supported crystalline and polycrystalline $PtSe_2$ thin films of varying thickness (1 to 40 layers), which were grown by molecular beam epitaxy (MBE) on zinc oxide (ZnO) substrates. First, by using a combination of low-frequency Raman and pump-probe coherent phonon spectroscopies we investigate the layer-breathing modes (LBM) in $PtSe_2$ thin films and extract an effective out-of-plane elastic constant, a layer-dependent sound velocity, and the acoustic phonon lifetimes. Then, we focus on unraveling the impact of crystallinity and size effects on the cross-plane thermal conductivity of supported $PtSe_2$ thin films taking into account the interfacial thermal resistances in our multilayer sample geometry. Finally, we investigate the thermal conductivity by the first-principles Boltzmann transport equation (BTE) computing the harmonic and anharmonic force constants by density functional theory (DFT) to reveal the microscopic mechanism of heat transport in $PtSe_2$ thin films.

RESULTS AND DISCUSSION

Material growth, structural characterization, and phonon dynamics

Two $PtSe_2$ wedges were grown under ultrahigh vacuum (base pressure in the low 10^{-10} mbar range) in an MBE chamber equipped with a cryo-panel and a reflection high energy electron diffraction (RHEED) setup. For the crystalline $PtSe_2$ wedge, four monolayers of $PtSe_2$ were deposited by co-evaporating Pt and Se on the ZnO (0001) substrate kept at 450 °C. The resulting RHEED

---

[1]Catalan Institute of Nanoscience and Nanotechnology (ICN2), CSIC and BIST, Campus UAB, Bellaterra 08193 Barcelona, Spain. [2]Departamento de Física, Universidad Autónoma de Barcelona, Bellaterra 08193 Barcelona, Spain. [3]Department of Chemistry, University of California, Davis, CA 95616, United States. [4]Université Grenoble Alpes, CNRS, CEA, Grenoble INP, IRIG-Spintec, 38054 Grenoble, France. [5]ICREA, Passeig Lluis Companys 23, 08010 Barcelona, Spain. ✉email: alexandros.elsachat@icn2.cat; emigdio.chavez@icn2.cat

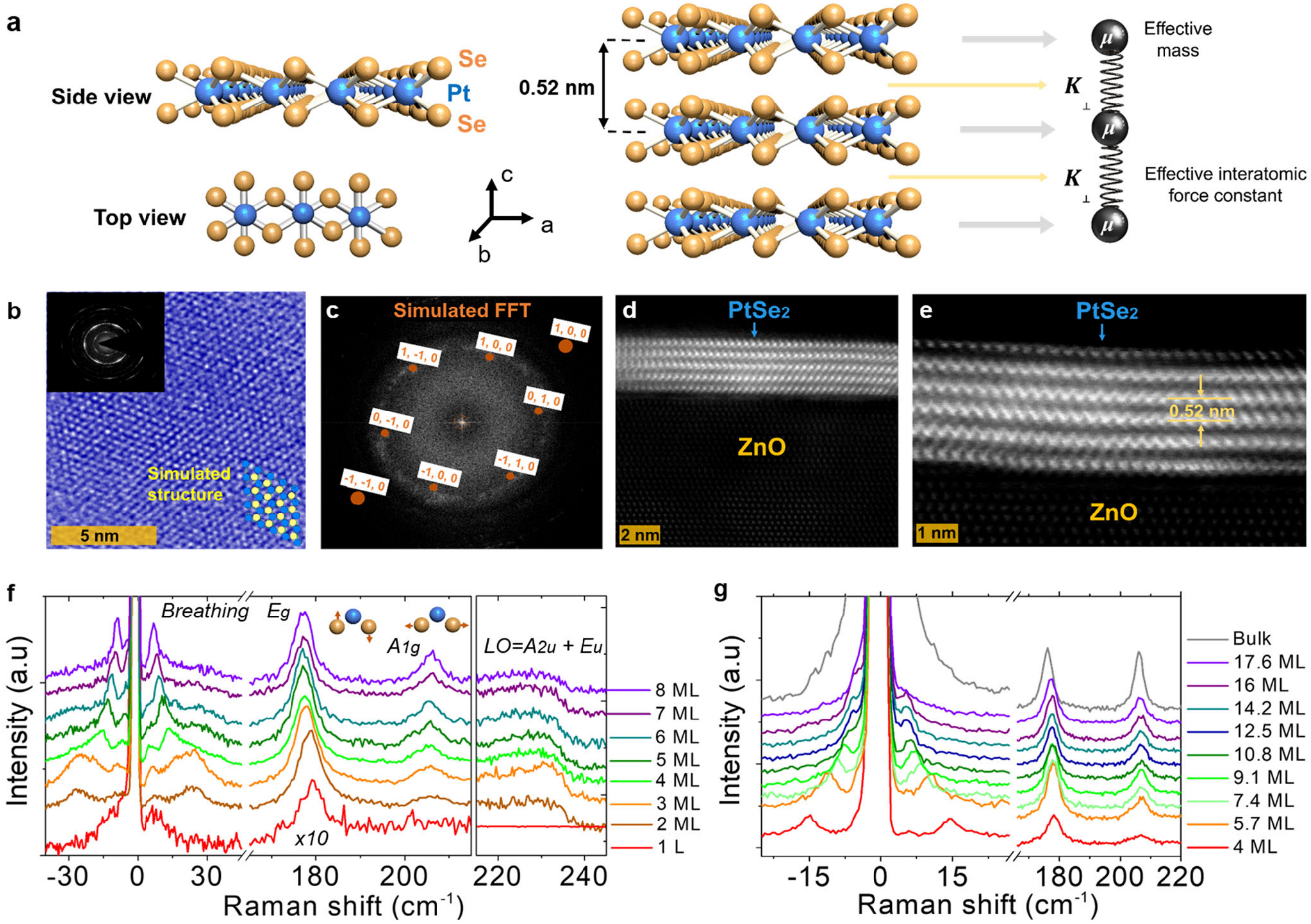

Fig. 1 Structural characterization and low-frequency Raman spectroscopy of $PtSe_2$. **a** Side and top views of the $PtSe_2$ crystal structure (left), schematics of the side view of a trilayer $PtSe_2$ crystal structure (middle), and the one-dimensional linear atomic chain model (right). The blue and orange spheres represent Pt and Se atoms, respectively. **b** HR-STEM images of a 5 ML crystalline $PtSe_2$ film and **c** the Fast Fourier transform of the respective image, from which we extract the *a* and *b* lattice constants, $a = b \approx 0.37$ nm. **d, e** Cross-sectional TEM images of the as-grown 3 nm (5 ML) $PtSe_2$ film, from which we extract the *c*-lattice constant, $c \approx 0.52$ nm. The $PtSe_2$ is layered and each layer is parallel to the underlying ZnO substrate. Thickness-dependent Raman spectra of **f** crystalline and **g** polycrystalline $PtSe_2$ films deposited on ZnO. The inset in (**f**) shows blue and orange spheres that represent Pt and Se atoms, respectively and arrows that point to the direction of the movement of that layer.

patterns were anisotropic with a 7° of mosaicity (see Supplementary Fig. 1), demonstrating the good-crystalline character of the film, and the epitaxy relationship was found to be ZnO (0001) [100]/$PtSe_2$ (111) [100]. Additional characterization of epitaxial ZnO/$PtSe_2$ is reported in reference [11]. For the polycrystalline $PtSe_2$ wedge, we first deposited a 2.4-Å-thick Pt film by magnetron sputtering at room temperature and selenized it in the MBE chamber by deposition of Se at room temperature and subsequent annealing at 750 °C under Se flux. The magnetron sputtering reactor and the MBE chamber are being connected under ultrahigh vacuum and $PtSe_2$ films are fully grown in situ. After selenization, the equivalent $PtSe_2$ thickness was two monolayers (2 ML). The RHEED patterns were streaky but isotropic, showing the in-plane polycrystalline character of the film, with a well-defined (0001) surface for all grains but random in-plane crystal orientation. Two more $PtSe_2$ films were finally deposited by co-evaporating Pt and Se at 450 °C to obtain a 4 ML thick polycrystalline film (see Supplementary Fig. 1c).

In a second step, we covered the sample with a motorized mechanical mask except for a thin 1.5-mm-large band at the edge to deposit 14 ML of $PtSe_2$ by co-evaporating Pt and Se at 450 °C. The mask was then retracted at a constant speed and stopped at 1 mm from the edge to evaporate the 0–22 ML $PtSe_2$ wedge by co-evaporation at the same temperature. We checked by RHEED that the films retained their respective crystalline and polycrystalline character at the end of the growth. The final structure is shown in Supplementary Fig. 1d. Each $PtSe_2$ monolayer consists of three atomic sublayers, in which Pt atoms are sandwiched between Se atoms (see Fig. 1a). Both samples were annealed at 750 °C for 10 min under Se flux after the growth in order to improve their crystalline quality. To avoid the film degradation during air transfer, the films were capped by a ~10-nm-thick amorphous Se layer deposited at room temperature.

The crystalline, acoustic and morphological characterizations of the samples were studied by Raman spectroscopy and high-resolution scanning transmission electron microscopy (HR-STEM) measurements. The arrangements of Pt and Se atoms in the planar HR-STEM image (Fig. 1b) and the symmetric diffraction pattern in the fast Fourier transform (FFT) image (Fig. 1c) further support the good crystal structure nature of the films. In addition, the high-magnification cross-sectional HR-STEM images (Fig. 1d, e) show the layered hexagonal honeycomb structure of a five layers $PtSe_2$ film, where bright Pt atoms are surrounded by six lighter colored Se atoms. The in-plane and out-of-plane lattice parameters were obtained from the (*l* 0 0) and (*l m* 0) planes of the FFT and image analysis of cross-plane sections of the film (see Fig. 1e), respectively.

The in-plane lattice constants were found to be $a = b \approx 0.37$ nm and $c \approx 0.52$ nm in good agreement with previous studies[10,15,19] and in excellent agreement with the ones deduced from our x-ray diffraction measurements (see Supplementary Fig. 2). On the other hand, DFT calculations give $a = 0.377$ nm and $c = 0.486$ nm. Whereas a is in excellent agreement with our measurements, c is significantly underestimated (6.5%). There may be multiple reasons for this discrepancy, among which the difficulty in the DFT calculations to simulate $PtSe_2$ and PtSe compounds for all the GGA exchange functionals (e.g., PBEsol, AM05)[20] and even van der Waals functionals (e.g., vdW-DF-C09 and vdW-DF-CX)[21].

The layered $PtSe_2$ adopts a T-type hexagonal crystal structure, belonging to the $P\bar{3}m1$ space group with a D_{3d} (-m) point group. The primitive $PtSe_2$ cell contains 3 atoms, then its vibrational spectrum includes nine modes: three acoustic ($A_{2u} + E_u$) and six optical ($A_{1g} + E_g + 2A_{2u} + 2E_u$). The optical modes can be classified as Raman active (E_g, A_{1g} and LO ($A_{2u} + E_u$)) and infrared active ($2E_u + 2A_u$) modes[22]. Fig. 1f, g show the Raman spectra of crystalline- and polycrystalline $PtSe_2$ films of different thicknesses, respectively. The high-frequency modes (170–210 cm^{-1}) are originated from in-plane and out-of-plane vibrations of Se atoms corresponding to E_g (~180 cm^{-1}) and A_{1g} (~205 cm^{-1}) modes, respectively. In addition, a weak interlayer longitudinal optical (LO) mode can be also observed at ~235 cm^{-1}. LO is generated by a combination of the in-plane E_u and out-of-plane A_{2u} modes from the vibrations of Pt and Se atoms in the opposite phases. The Raman peaks located in the low-frequency regions (−30 to 30 cm^{-1}) correspond to interlayer vibrations of $PtSe_2$ planes[5,18].

Specifically, the vibrations detected here are related to the out-of-plane displacements of the $PtSe_2$ layers known as layer-breathing modes (LBM). As shown in Fig. 1f, g, the position of the LBM shifts to lower frequencies as the number of layers increases. The thickness-dependence can be simulated by using a one-dimensional linear atomic chain model[23]. This model considers each $PtSe_2$ layer as a large atom with an effective mass per unit area $\mu = 4.8 \times 10^{-6}$ kg m^{-2} connected by a string with an effective interlayer breathing force constant (IBFC) per unit area $K_\perp$ and separated by a distance $d \approx 0.52$ nm given by the interatomic distance between layers (see Fig. 1a). The solution of the linear chain with vanishing stress as a boundary condition on the free surface is given by:

$$f = \sqrt{\frac{K_\perp}{\mu \pi^2}} \sin\left(\frac{q_{N,j}}{2} d\right) \qquad (1)$$

where f is the vibrational frequency of the mode, $q_{N,j} = 2\pi/\lambda_{N,j}$ is the acoustic wavevector, $\lambda_{N,j} = 2Nd/j$ is the phonon wavelength, N is the number of layers ($N = 2, 3, \ldots$) and j is the index of the acoustic mode ($j = 1, 2, 3\ldots$). The experimental and the fitted thickness-dependence of the first LBM ($j = 1$) is shown in Fig. 2a. The fitted curve was obtained using the IBFC adjustable variable, which is determined to be $K_\perp = 6.0 \pm 0.14 \times 10^{19}$ N m^{-3}. A similar value was also obtained by Chen et al.[18] with $K_\perp = 6.2 \times 10^{19}$ N m^{-3} using the same approach. Now, if we multiply the IBFC by the interlayer distance, we can also derive the corresponding C_{33} component of the elastic constant tensor[24,25].

For our system, we found $C_{33} = 31.8 \pm 0.95$ GPa, which is in the same range as other 2D materials e.g., 38.7–36.5 GPa for graphite, 54.3 GPa for $MoSe_2$[26], 24.5 GPa for h-BN[27], 52 GPa and 52.1 GPa for MoS_2 and WSe_2, respectively[25]. It is interesting to notice that the polycrystalline films also follow the same trend as the crystalline samples (see Fig. 2a) thus most likely the granular characteristics of the sample do not affect significantly the interlayers forces. Likewise, it is also possible to obtain the C_{44} constant using the effective interlayer shear force constant ($K_{//}$). Chen et al.[18]. calculated $K_{//} = 4.6 \times 10^{19}$ N m^{-3} for $PtSe_2$ based on density functional theory simulations from Zhao[5], giving $C_{44} = 23$ GPa and $v_{TA} = 1553$ ms^{-1}. In addition, from Eq. (1), it is also possible to

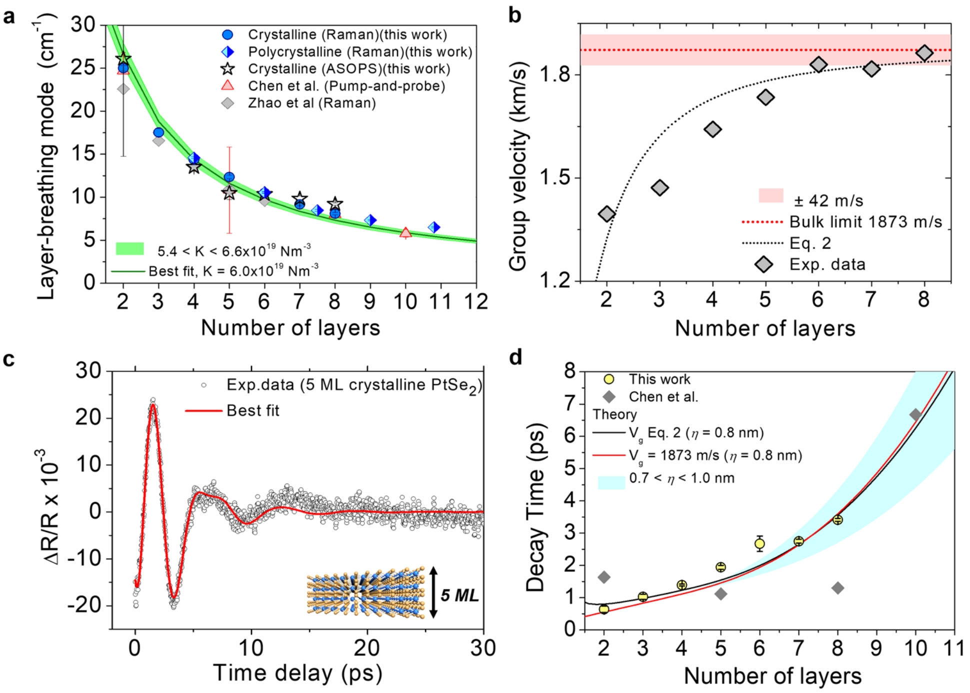

Fig. 2 **Phonon dynamics in $PtSe_2$. a** Peak position of the first order breathing mode measured in crystalline and polycrystalline $PtSe_2$ films using low-frequency Raman spectroscopy and ASOPS as a function of the number of layers and comparison with other experimental works. **b** Calculated group velocity as a function of the number of layers. **c** Representative transmission signal obtained with ASOPS in 5 ML $PtSe_2$ (black open circles) and the best fit (red line). **d** The extracted phonon decay time (yellow dots) vs the number of layers. The red and black curves are theoretical predictions of the phonon lifetimes based on the model proposed by Ziman[30]. The region displayed with light blue shows the impact of roughness in the calculated lifetimes. The gray data points show phonon lifetimes measured by Chen et al.[18].

extract the group velocity considering that $v_g = d(2\pi f)/dq$.

$$v_g = d\sqrt{\frac{K}{\mu}}\cos\left(\frac{\pi j}{2N}\right) \tag{2}$$

In the limit $N \to \infty$ and considering the experimental interlayer distance $d \approx 0.52 \pm 0.01$ nm, Eq. (2) gives the bulk limit for the cross-plane longitudinal velocity $v_{LA} = 1873 \pm 42\ \mathrm{ms}^{-1}$. A similar value can be obtained using an approximation of $v_g = \sqrt{\frac{C_{33}}{\rho}} = 1825 \pm 28\ \mathrm{ms}^{-1}$ where $\rho = 9540\ \mathrm{kg\ m}^{-3}$ is the density of $PtSe_2$ and $C_{33} = 31.8$ GPa. Using a numerical differentiation, it is also possible to extract the group velocity as a function of the number of layers as shown in Fig. 2b.

Furthermore, the phonon dynamics of the crystalline $PtSe_2$ samples were measured by pump-probe coherent phonon spectroscopy using the asynchronous optical sampling method (ASOPS)[28,29] (see details in Methods). Figure 2c shows the typical modulation of the reflectivity (ΔR/R) as a function of the time delay (black open circles) and the corresponding best model fit in a 5 ML $PtSe_2$ crystalline film. The change of reflectivity includes the effects of a fast and slow electronic relaxation process as well as the dynamics of the generated phonons. The time traces are fitted to a damped harmonic oscillator of the form:[18]

$$\Delta R/R = \sum_{i=1}^{2} A_i \exp\left(\frac{-t}{\tau_i}\right) + \sum_{j=1}^{2} B_j \exp\left(\frac{-t}{\tau_j}\right)\sin\left(2\pi f_j t + \phi_j\right) \tag{3}$$

where t is the time delay between the pump and the probe lasers, A and B are the amplitudes, τ_ι are the decay times, f the phonon frequency, and ϕ is a phase delay. The first term of Eq. (3) represents the fast and slow relaxation processes of the excited carriers. The second term describes the damped phonon oscillations. The Fast Fourier transforms (FFT) of the time-domain data for all measured samples are displayed in the Supplementary.

Figure 2d shows the measured decay time of LBM as a function of the number of layers (yellow dots) and the calculated phonon decay due to boundary scattering contribution based on the model proposed by Ziman[30]. This model considers the impact of the roughness (η) of the film surface through a phenomenological parameter $p = \exp[-16\pi^2\eta^2/\lambda^2]$, which modifies the effective mean free path $\Lambda = (1+p)/(1-p)\ Nd/v_g$ of the acoustic waves. The black and red curves of Fig. 2d were calculated using a thickness-dependent group velocity (Eq. (2)) and a constant value given by the bulk limit ($1873\ \mathrm{m\,s}^{-1}$), respectively, with a constant $\eta = 0.82$ nm as measured by AFM (see Supplementary Fig. 3).

Apart from the good agreement between the theory and the experimental data, we observe that the phonon lifetime is not affected by the group velocity (thickness-dependent or constant). Similar observations of boundary-limited lifetimes have been reported in suspended $MoSe_2$ flakes by Soubelet et al.[26]. They measured lifetimes of the order of ~1–41 ps in 2–8 ML limited by boundary effects. While in thicker samples (>20 ML), they observed longer lifetimes (~0.3–10 ns) limited by phonon-phonon scattering. The large difference in lifetimes measured here (1–4 ps) is mainly attributed to the difference in the phonon group velocity which is 1.4 to 1.5 times smaller than $MoSe_2$.

Thermal conductivity and interfacial heat transport measurements

For the thermal measurements, we used a custom-built frequency-domain thermo-reflectance (FDTR) setup, a well-established optical pump-probe technique, capable of measuring heat transport in thin films and across interfaces[31–36]. A schematic representation of the experimental setup is shown in Fig. 3a.

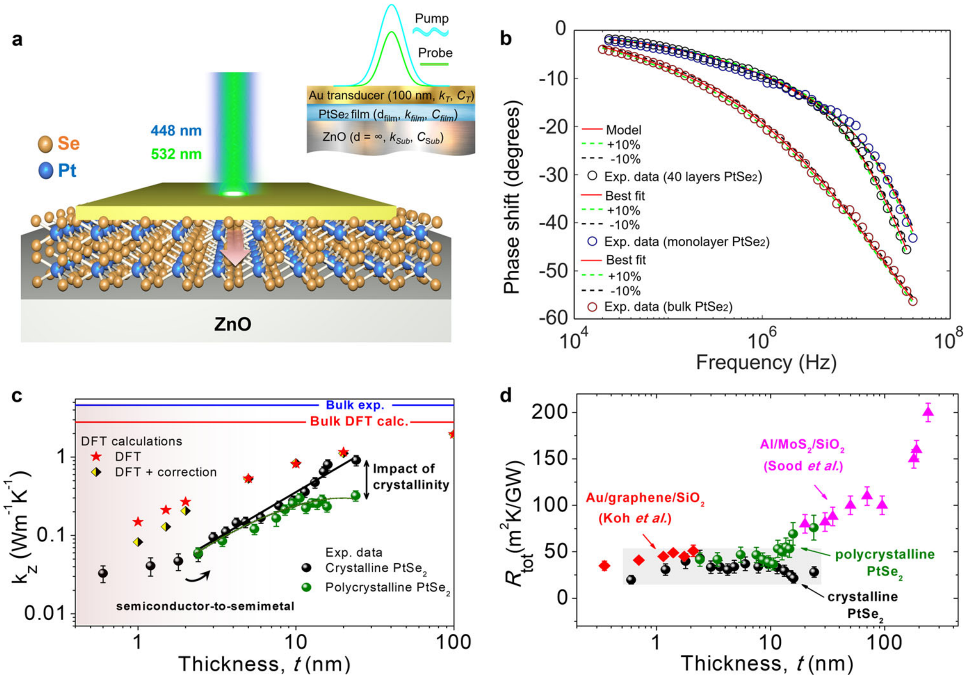

Fig. 3 Thermal conductivity and interfacial heat transport measurements. **a** Schematic illustrations of the FDTR technique and the multilayer system. **b** Typical FDTR data measured in bulk $PtSe_2$ (red circles), 40 layers (black circles), and monolayer (blue circles) crystalline $PtSe_2$ films and the corresponding best model fits in the whole frequency range. **c** Cross-plane thermal conductivity k_z of crystalline (black spheres) and polycrystalline (green spheres) $PtSe_2$ films versus film thickness t. The uncertainty of the estimated k_z was calculated based on error propagation for the input parameters. The blue and red lines in (**a**) display the bulk cross-plane thermal conductivity values obtained by FDTR and DFT calculations, respectively. The black and green curves are a guide for the eye. **d** Total thermal resistance, $R_{\mathrm{total}} = R_{\mathrm{int}} + R_{\mathrm{PtSe2}}$, of crystalline (black spheres) and polycrystalline (green spheres) $PtSe_2$ thin films, plotted versus film thickness t. The uncertainty region is displayed as a gray rectangle. The total cross-plane thermal resistance measurements of Au/graphene/SiO_2[47] (red diamonds) and Al/MoS_2/SiO_2[41] (purple triangles) interfaces are also reported.

A modulated pump beam with a wavelength of 448 nm is focused onto the sample, creating a periodic heat flux with a Gaussian spatial distribution on the sample surface. A reflected probe beam with a wavelength of 532 nm is aligned coaxially with the pump beam and focused with the pump spot to monitor the periodic fluctuations in reflectivity at the sample surface caused by the oscillating sample temperature. All the samples after the MBE growth were coated with a 100 nm thick Au layer, which was chosen to maximize the coefficient of thermo-reflectance at the probe wavelength ($\sim 2.36 \times 10^{-4}\,\mathrm{K}^{-1}$). We used a lock-in amplifier (Zurich Instruments HF2LI) to record the amplitude and phase response of the reflected probe beam to the thermal wave, and the phase lag between the pump and probe beam as the observable quantity. More details on the experimental setup can be found elsewhere[35].

In the present experiments, we obtained frequency-domain measurements by varying the modulation frequency of the pump beam over a wide range (20 kHz–40 MHz). The cross-plane thermal conductivity (k_z) of the $PtSe_2$ thin films was subsequently extracted by following a multilayer three-dimensional (3D) heat diffusion model that includes the interface thermal conductance between the different layers and anisotropic heat transport[31]. For each experiment, we quantified first the sensitivity of the recorded phase signal to different parameters: k_z, the volumetric heat capacity (C), the thermal conductivity anisotropy ratio (k_r/k_z), and the different interface thermal conductances, in a similar manner to that of Schmidt et al.[31]. The details about the measurement sensitivity to different combinations of parameters in the model can be found in Supplementary Fig. 4. In all the experiments we used a high-magnification 50× objective lens that produced a focused root mean square (rms) spot size ($1/e^2$ radius) of approximately ~1.5 µm. To reduce the uncertainties associated with variations in the laser spot size between measurements on different films, the spot size was measured for each different experiment using the knife's edge method, as shown in Supplementary Fig. 6. All the room temperature measurements were performed under both ambient and vacuum conditions.

Before the thermal measurements on thin $PtSe_2$ films, we performed FDTR measurements on a bulk $PtSe_2$ crystal coated with 100 nm of Au in order to extract the anisotropy ratio of the thermal conductivities. The thermal conductivity of the deposited Au film was first measured using electrical conductivity and the Wiedemann−Franz law, $k_{Au} = 195\,\mathrm{W m^{-1} K^{-1}}$ (see details in Supplementary Fig. 7). The volumetric specific heat of Au and $PtSe_2$ were taken from literature[10,36]. This leaves us with three unknowns: the cross-plane and in-plane thermal conductivity of the bulk $PtSe_2$ crystal and the Au-$PtSe_2$ interface thermal conductance ($G_{\text{Au-bulk}}$). The in-plane thermal conductivity was expressed in terms of the anisotropic ratio (α) and the cross-plane thermal conductivity $k_r = \alpha \cdot k_z$.

However, from the sensitivity analysis, we found that the recorded phase signal has low sensitivity to $G_{\text{Au-bulk}}$ and only at high frequencies while its sensitivity to the anisotropic heat flow is high in almost the whole frequency range (see Supplementary Fig. 5). This allowed us to extract α directly from the model fit of the experimental data in the low-frequency range (20 kHz–1 MHz) using a nonlinear least-squares routine, which requires an initial guess to determine the value of the free parameter (k_z) (see Supplementary Fig. 11). The inset in Supplementary Fig. 11 shows the numerical errors of the applied model fits as a function of different anisotropy ratios. The minimum value of the fitting error, which gives us the best fit of the FDTR data, corresponds to $\alpha = 9$, $k_z = 4.6 \pm 0.7\,\mathrm{W m^{-1} K^{-1}}$ and $k_r \approx 41.4\,\mathrm{W m^{-1} K^{-1}}$.

The observed anisotropy ratio between k_r and k_z in $PtSe_2$ is similar to previously reported values of other 2D-layered materials, such as InSe (α ~10)[37], $SnSe_2$ (α ~7–8)[35,38], and armchair black phosphorous (α ~6–10)[39]. Our first-principles BTE calculations give $k_z = 2.84\,\mathrm{W\,m^{-1}\,K^{-1}}$ and $k_r = 39.0\,\mathrm{W\,m^{-1}\,K^{-1}}$. k_r is in excellent agreement with the measurement, while k_z is significantly overestimated, possibly due to the discrepancy in the equilibrium c lattice parameter mentioned above. Nevertheless, we can still use DFT and BTE to analyse the phonon contributions to cross-plane transport in $PtSe_2$ bulk and the effect of finite thickness in thin films, at least qualitatively.

To study the impact of crystallinity and film thickness on the cross-plane thermal conductivity of $PtSe_2$ thin films, we performed FDTR measurements in large-area crystalline and polycrystalline $PtSe_2$ films of different thicknesses (1–40 ML) on ZnO substrate. The wedge sample stacks consist of Au/$PtSe_2$/ZnO (see Fig. 3a and Supplementary Fig. 1). Typical examples of the recorded phase signals and the corresponding best model fit for bulk, monolayer, and 40 ML crystalline $PtSe_2$ are shown in Fig. 3b. Here, the key parameters for the model in our multilayer system are the spot sizes of the pump and probe beams, k_z, the film thickness t, the C of each layer, and the interface thermal conductance (between Au and $PtSe_2$, G_1, and between $PtSe_2$ and ZnO, G_2). The thickness of Au and $PtSe_2$ films were measured by AFM and low-frequency Raman spectroscopy, respectively (see section above and Supplementary). The heat capacities of Au, ZnO, and $PtSe_2$ were taken from the literature[10,36,40]. Thus, the remaining unknown parameters were the k_z value of the $PtSe_2$ films, G_1 and G_2.

To extract a unique value of k_z from a single measurement we followed a fitting approach similar to that suggested in the previous works[31,32,35] and supported by our sensitivity analysis (see Supplementary Fig. 4). First, we estimate k_z by fitting to experimental data in a low-frequency range (20 kHz–1 MHz), where the measurement sensitivity to the G_1, G_2, and heat capacity of the films is negligible. Then, we fix k_z and fit experimental data in a high-frequency range (1–40 MHz) to estimate simultaneously G_1 and G_2. As an initial guess to determine the value of the free parameters (k_z, G_1, and G_2) we used previously reported values of similar material systems[41–43]. We also verified that the final fit results are not sensitive to the choice of initial values. The same analysis has been followed to extract k_z, G_1, and G_2 values for all the $PtSe_2$ films.

In Supplementary Fig. 13 we show all the interface thermal resistance measurements, $R_1 = 1/G_1$, $R_2 = 1/G_2$, and $R_{\text{int}} = R_1 + R_2$, extracted by the FDTR experiments. The observed variation of R_{int} might be attributed to differences in the interface characteristics of Au (transducer)/$PtSe_2$ and $PtSe_2$/ZnO (substrate), which could result in different interfacial energy coupling. The apparent increase of R_2 with increasing film thickness most likely is due to the reduced mechanical coupling of the films to the underlying ZnO resulting from a potential increase in sample stiffness or changes in the vibrational spectra[44]. However, we note that most of the extracted values are within the experimental uncertainty, thus it is not clear if there is a systematic increase of R_2 with thickness. Similarly, a weak thickness-dependent thermal resistance trend has been measured in InSe, MoS_2, and $SnSe_2$ thin films[35,37,41].

It is interesting to note that, in contrast to the bulk case, in FDTR measurements in thin films, the diameter of the laser spot is usually large compared to the thermal diffusion length during the modulation period of the pump beam. Thus, the heat flow is expected to be mainly one-dimensional in the cross-plane direction[32]. This has been confirmed by our sensitivity analysis, where we found that the sensitivity of the recorded phase signal to the in-plane transport is relatively low (see Supplementary Fig. 4c). Therefore, since anisotropic differences in thermal conductivities as a function of the film thickness cannot be resolved, for the data analysis we used the anisotropy ratio extracted from the bulk $PtSe_2$ experiments. The dependence of the thermal anisotropy with the film thickness has been studied recently in similar material systems, such as supported InSe[37] and $SnSe_2$[35] films, showing a thickness-independent α of 10 and 8.4, respectively.

Figure 3c displays the extracted k_z value of all the $PtSe_2$ thin films as a function of thickness. In both crystalline (black data points) and polycrystalline films (green data points), we observe a linear increase of k_z with increasing the film thickness starting from 2.4 nm (4 ML) up to 10 and 24 nm, respectively. In polycrystalline films with thicknesses $t > 12$ nm, k_z shows a plateau, and a maximum cross-plane thermal conductivity reduction of ~35% was observed compared to the crystalline samples. This result highlights the strong impact of crystallinity on k_z and suggests that depending on the film crystallinity phonons with different mean free paths (MFPs) contribute to k_z. In crystalline $PtSe_2$ films, heat is propagating through coherent vibrations (phonon modes) that travel distances at least 24 nm (~40 ML) while in polycrystalline samples, they start to decay above 12 nm (~20 ML). This behavior most likely is attributed to the enhanced phonon scattering due to the presence of high-density defective grain boundaries randomly oriented in the polycrystalline film. XRD measurements on polycrystalline films provided in Supplementary Fig. 12 confirmed the random orientation of the grains. On the contrary, as the film thickness becomes thinner ($t < 12$ nm), thermal phonons (especially long-wavelength phonons) are not strongly scattered by the reduced number of grain boundaries available within the volume of the materials, and both crystalline and polycrystalline films show similar k_z values.

In Fig. 3c, we also show the k_z obtained from first-principles DFT-BTE calculations, both, for bulk $PtSe_2$ and thickness-dependent values as two different sets of data. The first set accounts solely for the finite thickness of the film and gives an overall much larger thermal conductivity than the measured one at the corresponding thickness (red data points). The over-estimation of the calculated thermal conductivity for the whole thickness range can be related to the underestimation of the *c*-axis compared with the experimental data and the assumption of a perfect single-crystal structure of the films. In addition, G_1 and G_2 were not taken into account in the DFT calculations, which further explains the overestimated values in the calculated thickness-dependence of k_z. However, we observe that the trend of thickness-dependent of the thermal conductivity is preserved. Finally, correcting the BTE calculation for the observed thickness-dependent reduction of sound velocity provides a better agreement between theory and experiments over the whole range of thickness considered (yellow-black diamonds).

The observed linear dependence of k_z from four monolayers up to a certain thickness in both sets of samples is consistent with ballistic heat conduction processes, as has been shown in previous works, where the thermal conductivity increased linearly with the characteristic length of the system[41,45,46]. However, in few-layer crystalline $PtSe_2$ films ($t < 2$–3 nm), we observe a deviation from the linear thickness-dependence of k_z (see Fig. 3c, black spheres). Since interfaces might dominate cross-plane heat transport in very thin films, the apparent deviation might be attributed to variations in the total thermal resistance per unit area, R_{tot}, of the film (see calculations below), which can be written as the sum of the combined interface thermal resistance, $R_{int} = 1/G_1 + 1/G_2$, and volumetric cross-plane thermal resistance, $R_{PtSe2} = t/k_z$[41,47]. Note that this expression is not valid in very thin films and G_1 and G_2 should be treated as one diffusive interface instead of two discrete ones[41,47]. Another possible explanation for this deviation is the semiconductor-to-semimetal evolution of $PtSe_2$ films after 4 monolayers (~2 nm)[48], which might result in an additional contribution of the electron thermal conductivity to k_z and/or lower contact resistivity between $PtSe_2$ and Au[12].

To quantify the impact of cross-plane ballistic phonon transport on the total thermal resistance of multilayer $PtSe_2$ films, we plotted the total thermal resistance, $R_{tot} = R_{PtSe2} + R_{int}$, versus film thickness (Fig. 3d). We observe that in crystalline $PtSe_2$ R_{tot} remains almost constant in the entire thickness range (see black spheres), with values approximately of 28 ± 10 $m^2\,KGW^{-1}$, while in polycrystalline samples (see green spheres) R_{tot} is constant only up to 12 nm and then starts to increase up to 75 ± 10 $m^2\,KGW^{-1}$. The large contribution of the volumetric resistance component, R_{PtSe2}, to R_{tot} and the thickness-independent R_{tot} in crystalline films indicate ballistic phonon transport along the *c*-axis of the films. Similar results has been previously observed in few-layer-graphene and single-crystal MoS_2 flakes that showed a thickness-independent R_{tot} for film thicknesses between 0.4–4 nm[47] and 20–40 nm[41], respectively.

The increased values of R_{tot} in polycrystalline films after 12 nm indicate a transition from ballistic to diffusive transport regime most likely due to phonon grain boundary scattering. For comparison, in Fig. 3d we plot our calculated R_{tot} (black and green spheres) with previous total cross-plane thermal resistance measurements on different 2D materials, where similar interfacial contributions from the bottom (2D material/substrate) and top (metal/2D material) interfaces were taken into account[41,47]. Our values are in line with these estimations and suggest that in sufficiently thin films, phonons (especially long-wavelength phonons) can directly propagate between the metal and substrate without being strongly scattered by interfaces.

To further confirm the robustness of our approach to measuring the intrinsic cross-plane thermal conductivity of thin films, we performed Raman thermometry measurements in a few layers of crystalline $PtSe_2$ films (2, 3, and 4 layers of $PtSe_2$, see Supplementary Fig. 8), where we found k_z values in good agreement with the FDTR results (see Supplementary Table 1). The agreement between Raman and FDTR experiments further supports our R_{tot} calculations and shows that it is possible to quantify the interfacial thermal contributions in a multilayer structure from a single set of FDTR measurements despite the low phase sensitivity to G_1 and G_2. Note that in Raman thermometry measurements we have only the contribution of R_2 to the total thermal resistance.

Next, we estimate the room temperature phonon MFP in the cross-plane direction (Λ_z) using a simplified expression from the kinetic theory, $k_z \sim (1/3)C\upsilon_s\Lambda_z$, where υ_s is the averaged sound velocity of cross-plane acoustic modes. For $PtSe_2$ we used C ~1.78 MJ $m^{-3}\,K^{-1}$[49], while k_z and υ_s were determined experimentally ($k_z \sim 4.6\,Wm^{-1}\,K^{-1}$, $\upsilon_s \sim \sqrt[3]{\frac{1}{3}\left(\frac{1}{v_{LA}^3}+\frac{2}{v_{TA}^3}\right)}$) through our FDTR and ASOPS measurements described above. From this estimation, we found $\Lambda_z \sim 5$ nm, which corresponds to a thickness of approximately ten layers. However, our FDTR experimental data suggest that in crystalline $PtSe_2$ films phonons with $\Lambda_z > 24$ nm substantially contribute to the thermal conductivity (about 37% of the bulk value, from our BTE-DFT calculations) while in polycrystalline films grain boundary scattering reduces this value to ~12 nm (see Fig. 3c). This is in close agreement with our DFT calculations that show that phonons with MFP larger than 15 nm contribute to almost 55% of the total cross-plane bulk thermal conductivity (see Fig. 4a).

In particular, Fig. 4a shows the normalized cumulative thermal conductivity as a function of frequency (red axis) and phonon mean free path (black axis) for bulk $PtSe_2$. We observe a quite narrow cross-plane MFP distribution (1–200 nm) but longer than the rough estimation from the kinetic theory ~5 nm. This discrepancy is well known and comes from the fact that each phonon contributes in a different manner to the thermal conductivity[41,50–52]. An averaged value can be misleading and underestimate the real contribution of the phonon MFP to the total thermal conductivity. It is interesting to note also the rather large contribution (~30%) of low-frequency phonons (<1 THz) to the total thermal conductivity. These phonons modes are sensitive to the introduction of additional periodicity and their dispersion relation can be easily tuned through nanofabrication[53,54]. This opens the possibility of exploring alternative ways of tuning

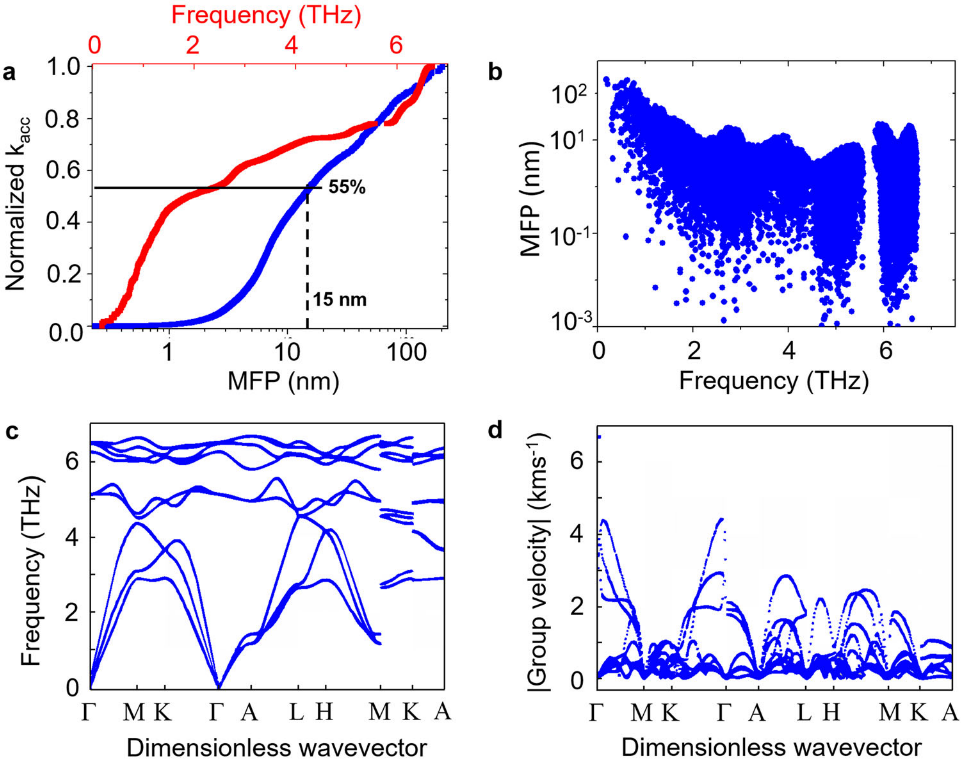

Fig. 4 First-principles DFT calculations. **a** Normalized thermal conductivity accumulation (k_{acc}) as a function of the phonon frequency (red curve) and MFP (blue curve) for bulk $PtSe_2$. **b** Calculated bulk phonon mean free as a function of frequency. **c** Phonon dispersion relations and **d** group velocity of bulk $PtSe_2$ along high-symmetry directions in the Brillouin zone.

thermal conduction through phonon engineering in two-dimensional materials.

Furthermore, in Fig. 4b we show that the MFPs in the cross-plane direction of the acoustic modes may be as high as 200 nm. Remarkably, there is a large number of optical modes with MFPs between 1 to 10 nm. This leads to a significant contribution of the optical modes to the thermal conductivity of bulk and $PtSe_2$ films, as shown in Fig. 4a and Supplementary Fig. 10. Finally, DFT-BTE calculations provide further insight into the heat transport mechanisms in $PtSe_2$. Figure 4c shows the phonon dispersions of bulk $PtSe_2$ along high-symmetry paths in the Brillouin Zone. As opposed to 2H phases, we observe no gap between the optical and the acoustic modes. It is worth noting that the high-frequency optical modes are unusually dispersive in the Γ-A direction if compared to other layered materials, for which optical phonons dispersions are usually flat[55]. This can be seen in Fig. 4d which displays the group velocities along the same k-point paths. Figure 4d also shows that the speed of sound in the Γ-A direction, averaged over the three acoustic branches, is 1930 m s^{-1} ($v_{LA} = 2120$ m s^{-1}).

In conclusion, we have studied phonon dynamic properties and heat transport in MBE-grown crystalline and polycrystalline $PtSe_2$ thin films of varying thickness (1 to 40 ML) using a combination of characterization techniques, i.e., FDTR, low-frequency Raman, and pump-probe coherent phonon spectroscopies, and state-of-the-art DFT calculations. Our work demonstrates the ability to quantify the influence of thickness and crystallinity on the cross-plane heat propagation in thin layered $PtSe_2$ films, showing an almost 35% reduction in the thermal conductivity of polycrystalline films with thickness larger than 12 nm in comparison with crystalline films of the same thickness. Moreover, from the phonon dynamic study in crystalline $PtSe_2$, we extract an out-of-plane elastic constant $C_{33} =$ 31.8 GPa and a layer-dependent group velocity ranging from 1340 ms^{-1} in bilayer $PtSe_2$ to 1873 ms^{-1} in eight layers of $PtSe_2$. Last, we showed that acoustic phonons in $PtSe_2$ thin films, which are the main carriers of heat in semiconductors, have extraordinarily short lifetimes in the order of picoseconds. Our results provide new insight into the heat transport and phonon dynamics in 2D materials at the nanoscale, with potential implications for the future design of 2D-based devices for energy harvesting and effective heat dissipation in thermoelectric and optoelectronic devices.

METHODS

Molecular beam epitaxy growth

Pt and Se were respectively evaporated thanks to an e-gun evaporator and a standard effusion cell. The Pt deposition rate was set to 0.75 Å min^{-1} and monitored in real-time by a quartz crystal microbalance. The pressure of Se at the sample position was measured with a retractable ionization gauge and set to 1.0×10^{-6} mbar, which corresponds to a Se:Pt flux ratio of about 15. The MBE reactor is connected under UHV to a magnetron sputtering chamber with a Pt target. The Pt deposition rate was set to 4.7 Å min^{-1} thanks to a retractable quartz crystal microbalance, the DC magnetron power was 1 W, and the argon pressure was 1.2×10^{-2} mbar. The ZnO (0001) substrates (CrysTec GmbH) were first etched for 30 s with an HCl 1.8% solution and rinsed with deionized water. This chemical treatment was followed by annealing for 1 h at 900 °C in an O_2 atmosphere, then annealing in UHV for 5 min at ~800 °C.

X-ray diffraction measurements

Grazing-incidence x-ray diffraction measurements were performed with a SmartLab Rigaku diffractometer. The source is a rotating anode beam tube (Cu Kα = 1.54 Å) operating at 45 kV and 200 mA. The diffractometer is equipped with a parabolic multilayer mirror and in-plane collimators of 0.5° on both source and detector sides defining the angular resolution. A Kβ filter on the detector side eliminates parasitic radiations.

Density functional theory calculations

We computed the lattice thermal conductivity of 1 T (octahedral) $PtSe_2$ by density functional theory (DFT) and the Boltzmann transport equation (BTE). In the DFT calculations, we used a van der Waals density functional with consistent exchange (vdW-DF-CX) that reliably predicts the structural and vibrational properties of several 2D materials, including transition metal dichalcogenides[56,57]. Valence Kohn-Sham wavefunctions are expanded on plane-waves basis set with a cutoff of 40 Ry, and projector augmented pseudopotentials are used to model screened nuclei[58]. A uniform $8 \times 8 \times 6$ mesh of k-points was used to integrate the first Brillouin Zone. Phonon dispersion relations were computed by density functional perturbation theory interpolating a uniform $4 \times 4 \times 3$ q-point mesh[59,60].

Boltzmann transport equation

Second-order and third-order force constants for the thermal conductivity calculations were computed by fitting the forces of 80 configurations of the $4 \times 4 \times 3$ $PtSe_2$ supercells, in which the atoms are randomly displaced with a standard deviation of 0.01 Å using the hiPhive code[61]. Second-order and third-order force constants were cut off at 6.9 and 5.13 Å, respectively. Fitting employed recursive feature elimination with a limit of 300 features (out of 961). The fit gives a root mean square error on the forces of 0.0044 eV/A with $R^2 = 0.999$. The solution of the linearized phonon BTE was computed by directly inverting the scattering tensor on a $21 \times 21 \times 17$ mesh of q-points, as implemented in kALDo[62]. The effect of the finite thickness of the samples is taken into account by including the boundary conditions in the scattering term as proposed by Maassen and Lundstrom[63].

Asynchronous optical sampling measurements

In this technique, two pulsed lasers (pump and probe beams) are focused on the sample surface. The pump produces a change of reflectivity which is measured by the probe beam as a function of the time delay between the lasers. The absorption of the pump laser causes an increase in the local strain via two separate mechanisms, namely thermal expansion, and the hydrostatic deformation potential. The thermal expansion is a consequence of the anharmonicity of the lattice, whereas the deformation potential is due to the excitation of electrons into binding orbitals. Both mechanisms periodically change the effective volume of the material, which in turn modulates the optical properties of the film that are probed by the second laser. In this experiment, we used 2 fs Ti:sapphire lasers with a repetition rate of ~1 GHz stabilized via an electronic feedback loop to achieve a small repetition rate difference of 2 kHz. The rate difference produces a time delay between the pump and probe pulses without the need for a mechanical delay stage. The delay between the pump pulses is kept at 1 ns, while the pump and probe pulses coincide every 500 ms. The measurements were done at a fixed central wavelength of λ = 790 nm for the pump (~1 mW) and the probe (~0.15 mW) beams, collinearly focused to a ~1-µm-diameter spot on the sample surface.

DATA AVAILABILITY

All relevant data and codes are available from the corresponding author on request.

Received: 6 December 2021; Accepted: 28 April 2022;

REFERENCES

1. Ferrari, A. C. et al. Science and technology roadmap for graphene, related two-dimensional crystals, and hybrid systems. *Nanoscale* **7**, 4598–4810 (2015).
2. Jariwala, D. et al. Gate-tunable carbon nanotube-MoS2 heterojunction p-n diode. *Proc. Natl Acad. Sci. USA* **110**, 18076–18080 (2013).
3. Massicotte, M. et al. Picosecond photoresponse in van der Waals heterostructures. *Nat. Nanotechnol.* **11**, 42–46 (2016).
4. Chhowalla, M., Jena, D. & Zhang, H. Two-dimensional semiconductors for transistors. *Nat. Rev. Mater.* **1**, 16052 (2016).
5. Zhao, Y. et al. High-electron-mobility and air-stable 2D layered PtSe2 FETs. *Adv. Mater.* **29**, 1604230 (2017).
6. Deng, Y. et al. Black phosphorus–monolayer MoS2 van der Waals heterojunction p–n diode. *ACS Nano* **8**, 8292–8299 (2014).
7. Yu, X. et al. Atomically thin noble metal dichalcogenide: a broadband mid-infrared semiconductor. *Nat. Commun.* **9**, 1545 (2018).
8. Liu, Y., Zhang, S., He, J., Wang, Z. M. & Liu, Z. Recent progress in the fabrication, properties, and devices of heterostructures based on 2D materials. *Nano Micro Lett.* **11**, 13 (2019).
9. Li, D. et al. Recent progress of two-dimensional thermoelectric. *Mater. Nano Micro Lett.* **12**, 36 (2020).
10. Gong, Y. et al. Two-dimensional platinum diselenide: synthesis, emerging applications, and future challenges. *Nano Micro Lett.* **12**, 174 (2020).
11. Bonell, F. et al. High carrier mobility in single-crystal PtSe 2 grown by molecular beam epitaxy on ZnO(0001). *2D Mater.* https://doi.org/10.1088/2053-1583/ac37aa (2021).
12. Yim, C. et al. Electrical devices from top-down structured platinum diselenide films. *npj 2D Mater. Appl.* **2**, 5 (2018).
13. Zhang, W., Qin, J., Huang, Z. & Zhang, W. The mechanism of layer number and strain dependent bandgap of 2D crystal PtSe2. *J. Appl. Phys.* **122**, 205701 (2017).
14. Wang, Y. et al. Monolayer PtSe2, a new semiconducting transition-metal-dichalcogenide, epitaxially grown by direct selenization of Pt. *Nano Lett.* **15**, 4013–4018 (2015).
15. Moon, H. et al. Strong thermopower enhancement and tunable power factor via semimetal to semiconductor transition in a transition-metal dichalcogenide. *ACS Nano* **13**, 13317–13324 (2019).
16. Guo, S.-D. Biaxial strain tuned thermoelectric properties in monolayer PtSe2. *J. Mater. Chem. C.* **4**, 9366–9374 (2016).
17. Yin, S. et al. Thermal conductivity of few-layer PtS 2 and PtSe 2 obtained from optothermal Raman spectroscopy. *J. Phys. Chem. C.* **125**, 16129–16135 (2021).
18. Chen, X. et al. Direct observation of interlayer coherent acoustic phonon dynamics in bilayer and few-layer PtSe 2. *Photonics Res.* **7**, 1416 (2019).
19. Zhang, K. et al. Experimental evidence for type-II Dirac semimetal in PtSe2. *Phys. Rev. B* **96**, 125102 (2017).
20. Cooper, V. R. Van der Waals density functional: an appropriate exchange functional. *Phys. Rev. B* **81**, 161104 (2010).
21. Terentjev, A. V., Constantin, L. A. & Pitarke, J. M. Dispersion-corrected PBEsol exchange-correlation functional. *Phys. Rev. B* **98**, 214108 (2018).
22. O'Brien, M. et al. Raman characterization of platinum diselenide thin films. *2D Mater.* **3**, 021004 (2016).
23. Luo, N. S., Ruggerone, P. & Toennies, J. P. Theory of surface vibrations in epitaxial thin films. *Phys. Rev. B* **54**, 5051–5063 (1996).
24. Carpinteri, A. *Structural Mechanics* (CRC Press, 2014).
25. Zhao, Y. et al. Interlayer breathing and shear modes in few-trilayer MoS2 and WSe2. *Nano Lett.* **13**, 1007–1015 (2013).
26. Soubelet, P. et al. The lifetime of interlayer breathing modes of few-layer 2H-MoSe 2 membranes. *Nanoscale* **11**, 10446–10453 (2019).
27. Jiménez-Riobóo, R. J. et al. In- and out-of-plane longitudinal acoustic-wave velocities and elastic moduli in h-BN from Brillouin scattering measurements. *Appl. Phys. Lett.* **112**, 051905 (2018).
28. Elzinga, P. A., Lytle, F. E., Jian, Y., King, G. B. & Laurendeau, N. M. Pump/probe spectroscopy by asynchronous optical sampling. *Appl. Spectrosc.* **41**, 2–4 (1987).
29. Bartels, A. et al. Ultrafast time-domain spectroscopy based on high-speed asynchronous optical sampling. *Rev. Sci. Instrum.* **78**, 35107 (2007).
30. Ziman, J. M. *Electrons and Phonons. The Theory of Transport Phenomena in Solids* (Oxford Univ. Press, 1960).
31. Schmidt, A. J., Cheaito, R. & Chiesa, M. A frequency-domain thermoreflectance method for the characterization of thermal properties. *Rev. Sci. Instrum.* **80**, 094901 (2009).
32. Schmidt, A. J., Chen, X. & Chen, G. Pulse accumulation, radial heat conduction, and anisotropic thermal conductivity in pump-probe transient thermoreflectance. *Rev. Sci. Instrum.* **79**, 114902 (2008).
33. El Sachat, A., Alzina, F., Sotomayor Torres, C. M. & Chavez-Angel, E. Heat transport control and thermal characterization of low-dimensional materials: a review. *Nanomaterials* **11**, 175 (2021).
34. Sandell, S. et al. Thermoreflectance techniques and Raman thermometry for thermal property characterization of nanostructures. *J. Appl. Phys.* **128**, 131101 (2020).
35. Xiao, P. et al. Anisotropic thermal conductivity of crystalline layered SnSe 2. *Nano Lett.* **21**, 9172–9179 (2021).
36. Sandell, S. et al. Enhancement of thermal boundary conductance of metal–polymer system. *Nanomaterials* **10**, 670 (2020).
37. Rai, A., Sangwan, V. K., Gish, J. T., Hersam, M. C. & Cahill, D. G. Anisotropic thermal conductivity of layered indium selenide. *Appl. Phys. Lett.* **118**, 73101 (2021).
38. Wang, H., Gao, Y. & Liu, G. Anisotropic phonon transport and lattice thermal conductivities in tin dichalcogenides SnS2 and SnSe2. *RSC Adv.* **7**, 8098–8105 (2017).
39. Jang, H., Wood, J. D., Ryder, C. R., Hersam, M. C. & Cahill, D. G. Anisotropic thermal conductivity of exfoliated black phosphorus. *Adv. Mater.* **27**, 8017–8022 (2015).
40. Serrano, J. et al. Heat capacity of ZnO: isotope effects. *Phys. Rev. B* **73**, 94303 (2006).
41. Sood, A. et al. Quasi-ballistic thermal transport across MoS2 thin films. *Nano Lett.* **19**, 2434–2442 (2019).

42. Subramanyan, H., Kim, K., Lu, T., Zhou, J. & Liu, J. On the importance of using exact full phonon dispersions for predicting interfacial thermal conductance of layered materials using diffuse mismatch model. *AIP Adv.* **9**, 115116 (2019).
43. Liu, X., Zhang, G. & Zhang, Y.-W. Thermal conduction across the one-dimensional interface between a MoS2 monolayer and metal electrode. *Nano Res.* **9**, 2372–2383 (2016).
44. Borlido, P., Huran, A. W., Marques, M. A. L. & Botti, S. Structural prediction of stabilized atomically thin tin layers. *npj 2D Mater. Appl.* **3**, 21 (2019).
45. Hsiao, T.-K. et al. Observation of room-temperature ballistic thermal conduction persisting over 8.3 µm in SiGe nanowires. *Nat. Nanotechnol.* **8**, 534–538 (2013).
46. Vakulov, D. et al. Ballistic phonons in ultrathin nanowires. *Nano Lett.* **20**, 2703–2709 (2020).
47. Koh, Y. K., Bae, M.-H., Cahill, D. G. & Pop, E. Heat conduction across monolayer and few-layer graphenes. *Nano Lett.* **10**, 4363–4368 (2010).
48. Ansari, L. et al. Quantum confinement-induced semimetal-to-semiconductor evolution in large-area ultra-thin PtSe2 films grown at 400 °C. *npj 2D Mater. Appl.* **3**, 33 (2019).
49. Maregedze, C. N. *Numerical Simulation of Structural Electronic, Optical and Thermal Properties of Platinium Dichalcogenides*. MSc thesis, Univ. of Witwatersrand. (2019).
50. Cuffe, J. et al. Reconstructing phonon mean-free-path contributions to thermal conductivity using nanoscale membranes. *Phys. Rev. B* **91**, 245423 (2015).
51. Henry, A. S. & Chen, G. Spectral phonon transport properties of silicon based on molecular dynamics simulations and lattice dynamic. *J. Comput. Theor. Nanosci.* **5**, 141–152 (2008).
52. Esfarjani, K., Chen, G. & Stokes, H. Heat transport in silicon from first-principles calculations. *Phys. Rev. B* **84**, 085204 (2011).
53. Graczykowski, B. et al. Phonon dispersion in hypersonic two-dimensional phononic crystal membranes. *Phys. Rev. B* **91**, 75414 (2015).
54. Sledzinska, M. et al. 2D phononic crystals: progress and prospects in hypersound and thermal transport engineering. *Adv. Funct. Mater.* **30**, 1904434 (2019).
55. Mortazavi, B. et al. Exploring phononic properties of two-dimensional materials using machine learning interatomic potentials. *Appl. Mater. Today* **20**, 100685 (2020).
56. Berland, K. & Hyldgaard, P. Exchange functional that tests the robustness of the plasmon description of the van der Waals density functional. *Phys. Rev. B* **89**, 035412 (2014).
57. Lindroth, D. O. & Erhart, P. Thermal transport in van der Waals solids from first-principles calculations. *Phys. Rev. B* **94**, 115205 (2016).
58. Blöchl, P. E. Projector augmented-wave method. *Phys. Rev. B* **50**, 17953–17979 (1994).
59. Baroni, S., de Gironcoli, S., Dal Corso, A. & Giannozzi, P. Phonons and related crystal properties from density-functional perturbation theory. *Rev. Mod. Phys.* **73**, 515–562 (2001).
60. Giannozzi, P. et al. Advanced capabilities for materials modelling with Quantum ESPRESSO. *J. Phys. Condens. Matter* **29**, 465901 (2017).
61. Eriksson, F., Fransson, E. & Erhart, P. The hiphive package for the extraction of high-order force constants by machine learning. *Adv. Theory Simul.* **2**, 1800184 (2019).
62. Barbalinardo, G., Chen, Z., Lundgren, N. W. & Donadio, D. Efficient anharmonic lattice dynamics calculations of thermal transport in crystalline and disordered solids. *J. Appl. Phys.* **128**, 135104 (2020).
63. Maassen, J. & Lundstrom, M. Steady-state heat transport: ballistic-to-diffusive with Fourier's law. *J. Appl. Phys.* **117**, 035104 (2015).

ACKNOWLEDGEMENTS

This work has been supported by the Severo Ochoa program, the Spanish Research Agency (AEI, grant no. SEV-2017-0706), and the CERCA Program/Generalitat de Catalunya. The authors acknowledge support from the Spanish MICINN project SIP (PGC2018-101743-B-I00), and the EU project NANOPOLY (GA 289061). The LANEF framework (ANR-10-LABX-51-01) is acknowledged for its support of mutualized infrastructure. PX acknowledges support for the Ph.D. fellowship from the EU Marie Sklodowska-Curie COFUND PREBIST (Grant Agreement 754558). AES acknowledges support by the H2020-MSCA-IF project THERMIC-GA No. 101029727. The authors acknowledge Dr. John Cuffe for his critical comments.

AUTHOR CONTRIBUTIONS

A.E.S. and E.C.-A., conceived the project. A.E.S. and E.C.-A., built the F.D.T.R., setup and performed the thermal measurements and data analysis. A.E.S. performed the A.F.M. measurements. E.C.-A. and P.X., performed the Raman measurements. E.C.-A. and G.A., performed the A.S.O.P.S., measurements and analysis. F.B., A.M., C.V., H.B. and M.J. fabricated the M.B.E. samples and performed the X.R.D., measurements. P.X., M.S., A.E.S. and E.C.-A., performed the T.E.M., measurements and the structural analysis. D.D. and Z.C., performed the D.F.T., calculations and provided support to the theoretical analysis. All authors reviewed and edited the manuscript and have given approval to the final version of the manuscript. The manuscript was written by A.E.S. and E.C.-A., A.E.S. and P.X., contributed equally.

COMPETING INTERESTS

The authors declare no competing interests.

ADDITIONAL INFORMATION

Supplementary information The online version contains supplementary material available at https://doi.org/10.1038/s41699-022-00311-x.

Correspondence and requests for materials should be addressed to Alexandros El Sachat or Emigdio Chavez-Angel.

Reprints and permission information is available at http://www.nature.com/reprints

Publisher's note Springer Nature remains neutral with regard to jurisdictional claims in published maps and institutional affiliations.